Theoretical and empirical analysis of the average cross-sectional areas of breakup fragments

Hanada, Toshiya
Department of Aeronautics and Astronautics, Kyushu University

Liou, J.-C.
NASA/JSC, Mail Code KX, 2101 NASA Parkway, Houston

出版情報：Advances in Space Research. 47 (9), pp.1480-1489, 2011-05-03. Elsevier
バージョン：

Theoretical and Empirical Analysis of the Average Cross-sectional Areas of Breakup Fragments

T. Hanada[a1], J.-C. Liou[b]

[a]*Kyushu University, 744 Motooka, Nishi-ku, Fukuoka 819-0395, JAPAN*
[b]*NASA/JSC, Mail Code KX, 2101 NASA Parkway, Houston, TX 77058, USA*

Abstract

This paper compares two different approaches to calculate the average cross-sectional area of breakup fragments. The first one is described in the NASA standard breakup model 1998 revision. This approach visually classifies fragments into several shapes, and then applies formulae developed for each shape to calculate the average cross-sectional area. The second approach was developed jointly by the Kyushu University and the NASA Orbital Debris Program Office. This new approach automatically classifies fragments into plate- or irregular-shapes based on their aspect ratio and thickness, and then applies formulae developed for each shape to calculate the average cross-sectional area. The comparison between the two approaches is demonstrated in the area-to-mass ratio (*A/m*) distribution of fragments from two microsatellite impact experiments completed in early 2008. A major difference between the two approaches comes from the calculation of the average cross-sectional area of plates. In order to determine which of the two approaches provides a better description of the actual *A/m* distribution of breakup fragments, a theoretical analysis in the calculation of the average cross-sectional area of an ideal plate is conducted. This paper also investigates the average cross-sectional area of multi-layer insulation fragments. The average cross-sectional area of 214 multi-layer insulation fragments was measured by a planimeter, and then the data were used to benchmark the average cross-sectional areas estimated by the two approaches. The uncertainty in the calculation of the average cross-sectional area with the two approaches is also discussed in terms of size and thickness.

Keywords: Space debris; Impact fragmentation; Estimate; Area-to-mass ratio

1. Introduction

The average cross-sectional area and the area-to-mass ratio (*A/m*) of orbital debris are two key parameters needed for many environment modeling applications. For example, the former is directly related to collision probability calculation for the future population projection and the latter is related to the orbital lifetime estimate for objects below approximately 1000 km altitude. Objects with high *A/m*s also experience strong solar radiation pressure perturbation and exhibit evolution patterns very different from those with low *A/m*s. Although the values of these two parameters for objects in the U.S. Space Surveillance Network (SSN) can be estimated from the radar cross section observations and objects' orbital history data, manual inspection and measurements of fragments generated from laboratory explosion or collision tests would still establish the ground truth. In addition, the SSN catalog is limited to objects 10 cm and larger. Analysis of the laboratory test fragments is the only way to obtain data for smaller objects.

The key laboratory test data used in the development of the NASA standard breakup model is the Satellite Orbital Debris Characterization Impact Test (SOCIT) conducted in 1990 (McKnight et al., 1995; Krisko et al., 2000; Johnson et al., 2001). Systematic classification, measurements, and analyses of about 10 % of the SOCIT fragments were conducted. The results were incorporated into the NASA standard breakup model, and the model has been validated and implemented into many orbital debris environment

[1] Corresponding author. Address: Department of Aeronautics and Astronautics, Kyushu University, 744 Motooka, Nishi-ku, Fukuoka 819-0395, Japan.
E-mail address: hanada.toshiya.293@m.kyushu-u.ac.jp (T. Hanada).

models for more than 10 years. Although the SOCIT test was a very successful experiment, the target satellite used was a U.S. Navy Transit Navigation satellite built in the early 1960s. However, because of technological advancements, very different materials, such as lightweight fiber composites, are commonly used in the fabrication of modern satellites. Fragments generated from the breakup of a modern satellite, such as Iridium 33, may show physical and orbital characteristics very different from those described by the NASA standard breakup model (Liou 2009).

To better understand the physical properties of fragments made of modern materials, Kyushu University and the NASA Orbital Debris Program Office have collaborated on a series of microsatellite impact tests since 2004. The objective is to explore the effects of different impact conditions on microsatellites and then measure and analyze the size, mass, average cross-sectional area, *A/m*, shape, and composition properties of the individual fragments. These microsatellites were made of modern construction materials and equipped with typical electronic components. In addition, in the two most recent tests, the target satellite exteriors were covered with multi-layer insulation (MLI). During the post-test analyses, it became clear there might be a need to re-analyze the methodology adopted in the SOCIT test, especially in the fragment shape classification and the calculation of the average cross-sectional area. This paper summarizes an effort to re-evaluate the SOCIT approach and to develop an alternative way to classify fragment shape and average cross-sectional area distributions. Both of these approaches were tested on the recent microsatellite impact fragments. Comparisons were also made with a theoretical analysis of ideal plates and with actual measurements of MLI fragments using a planimeter, an instrument for mechanically measuring the area of a plane figure.

2. NASA Approach

The approach described in the NASA standard breakup model was developed to analyze the SOCIT fragments. To estimate the average cross-sectional area of an irregular-shaped fragment, the procedure is to first determine the projected areas of the object in the *x*-*y* plane ($A_{x\text{-}y}$), in the *y*-*z* plane ($A_{y\text{-}z}$), and in the *z*-*x* plane ($A_{z\text{-}x}$), and then calculate the average cross-sectional area as

$$A_{irregular} = \frac{1}{3}\left(A_{x\text{-}y} + A_{y\text{-}z} + A_{z\text{-}x}\right) \tag{1}$$

Here *x* is the longest dimension, *y* is the longest dimension in the plane perpendicular to *x*, and *z* is the longest dimension perpendicular to both *x* and *y* (see also Krisko et al., 2008). Eq. (1) provides the arithmetic mean of the three projected areas so that prior shape classification in the three cross-sectional areas must be considered. Therefore, the NASA approach visually classifies SOCIT fragments into 1) flat plate, 2) curled plate, 3) box, 4) sphere, 5) flake, 6) rod, 7) cylinder, 8) box and plate, 9) "other," and 10) nugget. The SOCIT fragments were dominated by nuggets (59%), "others" (23%), and flakes (13%). They account for approximately 95 % of the analyzed SOCIT fragments. It may be noted that needle-like fragments from the microsatellite impact experiments were treated as cylinders in the analysis below.

The NASA approach proposes to treat shape types of flat plate, curled plate, and flake as plates and to use

$$A_{plate} = \frac{1}{2}\left(L_C^2 + 2L_C \times z\right) \tag{2}$$

where L_C is the characteristic length defined as the average of three orthogonal projection dimensions in *x*, *y*, and *z*. Eq. (2) was validated using fragments from three explosion tests that ESA European Space Operations Center performed on scale models of the Ariane H10 upper stage tank (Fucke et al., 1993). This approach was possible because all fragments from the tests were plate-shaped.

Regarding other shape types, the NASA approach proposes to treat irregular- and cylinder-shaped fragments as ellipsoids with a rhombus in the projected area in the *y*-*z* plane. With this treatment on shape type Eq. (1) becomes

$$A_{irregular} = \frac{2}{9}\left(x \times y + y \times z + z \times x\right) \tag{3}$$

3. New Approach

Hanada et al. (2009b) proposed a new approach to estimate the average cross-sectional area of breakup fragments. This new approach is slightly different from the analytic method adopted in the NASA standard breakup model. Hanada et al. (2009b) demonstrated that a simple and general transition between irregular- and plate-shaped regimes could be expressed as a function of the aspect ratio of *x* to y (*x/y*) and the aspect ratio of *y* to *z* (*y/z*). In general, a high value of *x/y* indicates a long, narrow fragment whereas a low value of *x/y* indicates a short, stubby fragment. Accordingly, the ratio of *x* to *y* is a measure of how long and slender the fragment appears as seen in the *x*-*y* plane. Similarly, a high value of *y/z* indicates a thin fragment whereas a low value of *y/z* indicates a thick fragment. Therefore, we describe the ratio of *y* to *z* as "thinness" so it can be distinguished from the *x/y* aspect ratio.

Fig. 1 illustrates the applicable regimes where fragments can be classified into irregular- or plate-shaped objects. It is assumed that any fragment shape can be represented by an ellipsoid. For an ellipsoid whose equatorial radii and polar radius are *x*/2, *y*/2, and *z*/2, respectively, the irregular-shaped formula given by Eq. (1) becomes

$$A_{irregular} = \frac{\pi}{12}\left(x \times y + y \times z + z \times x\right) \tag{4}$$

The error of each formula in the calculation of the average cross-sectional area can be estimated by comparing the value with the true average cross-sectional area of the ellipsoid in an approximate formula given by

$$A_{ellipsoid} = \frac{\pi}{4}\left(\frac{x^p y^p + y^p z^p + z^p x^p}{3}\right)^{\frac{1}{p}}$$

where p ~ 1.0675 yields a relative error of at most 1.061 % (see also Knud Thomsen's formula at http://en.wikipedia.org/wiki/Ellipsoid).

Fig. 1 may clearly demonstrate the limitation of the plate-shaped formula given by Eq. (2) to be applicable. Therefore, Fig. 1 is also applicable for this study to automatically classify fragments into irregular- or plate-shaped objects based on their two aspect ratios. The average cross-sectional areas of fragments appearing in the irregular-shaped regimes were estimated by Eq. (4). The average cross-sectional areas of fragments appearing in the plate-shaped regime (the shaded area) were estimated by Eq. (2).

4. The area-to-mass ratio distribution comparison

4.1. Impact Experiments

Table 1 and Fig. 2 summarize the seven microsatellite impact tests completed between 2004 and 2008. Three different target microsatellites were prepared for the experiments. The first two targets were 15 cm by 15 cm by 15 cm in size and 740 g in mass. The next five targets were 20 cm by 20 cm by 20 cm in size, slightly larger than the first two. As will be described later, a solar panel and MLI were added to the last two targets so that their masses became significantly higher.

As shown in Fig. 3, the main structure of each microsatellite was composed of five layers (top and bottom layers and three internal layers parallel to the top and bottom layers) and four side panels as well. They were assembled with angle bars made of an aluminum alloy and metal spacers. The top and bottom layers and side panels were made of carbon fiber reinforced plastic (CFRP), while the three internal layers were made of glass fiber reinforced plastic (GFRP). The interior of each microsatellite was equipped with

fully functional electronic devices, such as a wireless radio, lithium-ion batteries, and circuits for communication, electric power supply, and command and data handling.

Fig. 2 shows that the last two targets were equipped with a solar panel on the top layer. The solar panel included an aluminum honeycomb sandwich panel and a CFRP face sheet with six solar cells mounted to it. The four side panels and bottom layer were covered with MLI. The MLI consisted of six aluminum coated, thermal control films and lint-free wipes slipped in between the films as spacers.

Table 1 and Fig. 2 also summarize the impact parameters of all experiments. Two different sized, aluminum alloy solid spheres were prepared as projectiles for the first two experiments (labeled HVI and LVI) in order to investigate the outcome of hypervelocity and low-velocity impacts. One projectile was 1.4 cm in diameter and 4 g in mass with an impact speed of 4.44 km/s, whereas the other was 3 cm in diameter and 39 g in mass with an impact speed of 1.45 km/s. For the remainder, only the latter projectiles were prepared.

The third through fifth experiments were carried out to investigate the effects of impact direction. Therefore, the projectile of the third and fifth experiments (labeled 1 and 3, respectively) impacted the target satellites with a direction perpendicular to the internal layers of the satellites, whereas the projectile of the fourth experiment (labeled 2) impacted the target with a direction parallel to the internal layers. Regarding the impact speed, the third and fourth experiments (labeled 1 and 2) were the same (1.66 km/s), whereas the fifth experiment (labeled 3) was slightly faster (1.72 km/s).

The last two experiments were carried out to investigate MLI and solar panel pieces. The target was oriented so that the solar panel was facing the in-coming projectile in the sixth experiment (labeled F). In the last experiment (labeled R), on the other hand, the target was oriented so that the solar panel was on the opposite side of the impact surface.

The ratio of impact kinetic energy to target mass either exceeded 40 J/g or was slightly below 40 J/g. The NASA standard breakup model defines a collision, with a kinetic energy to target mass ratio equal to or greater than 40 J/g, to be catastrophic (see also Johnson et al., 2001). Therefore, the consequences of the experiments were expected to be catastrophic according to the NASA criterion. Actually, all target microsatellites were completely fragmented, consistent with the NASA prediction.

Details of the outcome of each impact experiment can be found in Hanada and Liou (2008), Hanada et al. (2009a), and Murakami et al. (2009). Here we focus on the last two experiments, F and R, to conduct a comparison between the NASA and present approaches in the calculation of the average cross-sectional area.

4.2. Fragment Shape Classification

Differences between the two approaches in shape classification are demonstrated using fragments from F and R, as listed in Table 1. Fig. 4 compares major fragments observed from F and R. The CFRP layer and side panel fragments are easily recognizable among the pieces, as are the MLI pieces. The overall characteristics are similar, although a significant difference in size and number between the MLI pieces can be observed. The largest MLI piece in F is similar in size to the CFRP layers or side panels, whereas larger MLI pieces were left in R. The projectile hit the solar panel to create more fragments in F, and then the fragments from the solar panel expanded and crashed into the side panels and MLI to create many more fragments. In contrast, the projectile hit the bottom CFRP layer and created fewer fragments in R.

As summarized in Table 1, 2400 fragments were collected from F, whereas 1250 fragments were collected from R. Each fragment was measured by three orthogonal projection dimensions and weight, and then visually classified into irregular- or plate-shaped. Fig. 5 clearly demonstrates that the majority of NASA's irregular-shaped fragments are classified as irregular-shaped by the present approach. Two major shape groups can be recognized in Fig. 5. One consists of fragments with a high value of x/y. Most of these fragments are needle-like fragments originating from the fragmentation of CFRP materials used to construct the microsatellites. The other group consists of fragments with relatively low values of x/y and y/z.

As clearly demonstrated in Fig. 6, many plates appear in the irregular-shaped regimes. The present approach treats these plates as irregular-shaped objects even though they are visually classified as plates. As will be discussed later, this difference in shape classification of visually classified plates causes a major difference in the area-to-mass ratio (A/m) distribution between the two approaches.

4.3. Area-to-mass Ratio Distribution

Differences in the area-to-mass ratio (*A/m*) distribution between the two approaches are also demonstrated using fragments from F and R, as listed in Table 1. Fig. 7 shows the *A/m* distribution of all fragments from F and R. The *A/m* distributions have two major peaks, corresponding to high- and low-density materials: (1) between 0.1 and 1 m^2/kg, and (2) between 1 and 10 m^2/kg. The former includes fragments with metallic components, whereas the latter includes CFRP pieces. Two more minor peaks can be observed in the *A/m* distributions: (1) near 10 m^2/kg, and (2) near 100 m^2/kg. These two minor peaks consist of the MLI pieces.

Regarding the difference between the two approaches in the calculation of the average cross-sectional of fragments, we can observe a major difference in the *A/m* distribution of fragments from F at a range of 1 and 10 m^2/kg, as demonstrated in Fig. 7. However, no significant difference can be observed from the *A/m* distribution of fragments from R. Figs. 5, 6, 8 and 9 indicate that the difference in the *A/m* distribution shown in Fig. 7 comes from prior shape classification and applied shape-dependent formulae.

First, most of the fragments visually classified as irregular-shaped objects appear in the irregular-shaped regime, as demonstrated in Fig. 5. Therefore, a difference may come from shape-dependent formulae that each approach adopted. Actually, Eq. (3), which the NASA approach adopted, slightly underestimates the average cross-sectional area of irregular-shaped fragments in comparison to Eq. (4), which the present approach adopted. However, no significant difference can be observed.

Secondly, as demonstrated in Fig. 6 (left), many fragments from F appear in the irregular-shaped regime even though they are visually classified as plates. The NASA approach applies the plate-shaped formula to fragments visually classified as plates. On the other hand, the present approach applies the irregular-shaped formula to these fragments. Therefore, as demonstrated in Fig. 9 (left), we can observe a significant difference in the *A/m* distribution of fragments. However, as demonstrated in Fig. 6 (right), not as many fragments from R appear outside the upper limit of the plate-shaped regime. Therefore, as demonstrated in Fig. 9 (right), we can observe no difference in the *A/m* distribution of fragments between the two approaches.

5. Theoretical Analysis of Average Cross-sectional Area

As demonstrated in the previous section, the major difference in the *A/m* distribution between the two approaches comes from the calculation of the average cross-sectional area of visually classified plates using each approach. In order to determine which of the two approaches provides a better description of the actual *A/m* distribution of breakup fragments, we conduct a theoretical analysis in the calculation of the average cross-sectional area of an ideal plate.

Let us consider a plate with a width of *w*, a depth of *d*, and a height of *h*, as illustrated in Fig. 10, to discuss which approach provides a better estimate of the average cross-sectional area of the plate. Here we assume that $w \geq d \geq h$ and $w^2 \geq \sqrt{d^2 + h^2}$. The total surface area of the plate is calculated by $2(d \times h + h \times w + w \times d)$. The average cross-sectional area of the plate, assumed to be one quarter of the total surface area, is calculated by

$$A_{ideal\ plate} = \frac{1}{2}(d \times h + h \times w + w \times d) \tag{5}$$

Fig. 10 defines the NASA orthogonal projection dimensions of *x*, *y*, and *z* for the plate. From Fig. 10 we can easily express the dimensions of *x*, *y*, and *z* in terms of *d*, *h*, and *w* as follows:

$$x = \sqrt{d^2 + h^2 + w^2}$$
$$y = \frac{2w\sqrt{d^2 + h^2}}{\sqrt{d^2 + h^2 + w^2}}$$
$$z = \frac{2dh}{\sqrt{d^2 + h^2}}$$

With the assumption made previously, we may be able to express w^2, d^2, and h^2 in the following forms:

$$w^2 = f_+(x, y)$$
$$d^2 = \frac{1}{2}\left(f_-(x, y) + \sqrt{f_-(x, y)\left(f_-(x, y) - z^2\right)}\right)$$
$$h^2 = \frac{1}{2}\left(f_-(x, y) - \sqrt{f_-(x, y)\left(f_-(x, y) - z^2\right)}\right)$$

where

$$f_\pm(x, y) = \frac{1}{2}x\left(x \pm \sqrt{x^2 - y^2}\right)$$

and $f_-(x, y) - z^2$ should be equal or greater than 0 to satisfy the assumptions made for this theoretical analysis.

The NASA standard breakup model proposes to use the plate-shaped formula given by Eq. (2) to estimate the average cross-sectional area of plates. Therefore, we may define the estimate uncertainty of the NASA approach in the calculation of the average cross-sectional area of plates by $\left|A_{plate} - A_{ideal\ plate}\right| / A_{ideal\ plate}$. Fig. 11 plots the estimate uncertainty of the plate-shaped formula given by Eq. (2) in the calculation of the average cross-sectional area of plates as a function of the aspect ratio (*x/y*) and thinness (*y/z*). Fig. 11 clearly demonstrates that the NASA approach is highly sensitive to the aspect ratio and that the estimate uncertainty increases drastically with the aspect ratio. Fig. 11 also demonstrates that the plate-shaped formula may overestimate the average cross-sectional area of thicker plates with a low value of *y/z*. Actually, as shown in Fig. 6, there are many plates with a high aspect ratio and thicker plates. The NASA approach may overestimate their average cross-sectional area.

As demonstrated in Fig. 1, the present approach classifies plates based on aspect ratio (*x/y*) and thinness (*y/z*). If a plate appears in the plate-shaped regime in Fig. 1, then the plate-shaped formula given by Eq. (2) is applied to estimate the average cross-sectional area of the plate. If not, on the other hand, the irregular-shaped formula is applied. The present approach proposes to treat plates appearing in the irregular-shaped regime as irregular-shaped objects even though these plates are visually classified as plates.

Similarly the uncertainty in the estimation of the average cross-sectional area, calculated by Eq. (4) according to the new approach, may be defined as $\left|A_{irregular} - A_{ideal\ plate}\right| / A_{ideal\ plate}$. Such estimate is plotted in Fig. 12, which clearly demonstrates that the Eq. (4) is insensitive. The estimate uncertainty is below approximately 32 %, even at the worst case, where values of *x/y* and *y/z* are 1 and $\sqrt{2}$, respectively.

By applying Fig. 1 to Figs. 11 and 12, we can plot the estimate uncertainty of the present approach in the calculation of the average cross-sectional area of plates, as demonstrated in Fig. 13. Comparison of Fig. 11 with Fig. 13 indicates that the present approach may provide a better estimate in the calculation of the average cross-sectional area of plates in the irregular-shaped regime. However, the present approach has high estimate uncertainty in the plate-shaped regime, especially along and near the upper limit of the plate-shaped regime. Therefore, there is an opportunity for improvement.

6. Empirical Analysis of Average Cross-sectional Area of MLI fragments

The average cross-sectional area of 214 MLI fragments from F and R listed in Table 1 was measured by the planimeter. Then, the measurement data were used to benchmark the average cross-sectional area estimated by the two approaches.

Fig. 14 compares the average cross-sectional area measured by the planimeter with those estimated by the two approaches. The dashed line in Fig. 14 represents the ideal average cross-sectional area, i.e., $A_{estimated} = A_{measured}$. Therefore, both approaches may overestimate the average cross-sectional area of MLI pieces.

Fig. 15 benchmarks the average cross-sectional area estimated by the two approaches in terms of the characteristic length (L_C) and thickness (z). Here we define error in the calculation of the average cross-sectional area by $\left(A_{estimated} - A_{measured}\right)/A_{measured}$. As clearly demonstrated in Fig. 15, there is no correlation between the estimate uncertainty and the characteristic length. On the other hand, a clear positive correlation between the estimate uncertainty and the thickness can be observed from Fig. 15. This clear correlation is because we assumed that each MLI piece is a flat plate figure to measure the surface area and to estimate the average cross-sectional area from the measured surface area. Therefore, since the thickness brings a higher estimate uncertainty, the estimate uncertainty increases with the thickness.

7. Conclusions

This paper compared two different approaches to calculate the average cross-sectional area of breakup fragments. The first approach is described in the NASA standard breakup model 1998 revision, whereas the second approach was developed jointly by Kyushu University and the NASA Orbital Debris Program Office. The comparison between the two approaches was demonstrated in the area-to-mass ratio distribution of fragments from microsatellite impact experiments completed in early 2008, and theoretically in the calculation of the average cross-sectional area of an ideal plate. This paper also investigated the average cross-sectional area of MLI pieces. The average cross-sectional area of 214 MLI pieces was measured, and then the data were used to benchmark the average cross-sectional areas estimated by the two approaches. The comparison and investigation presented in this paper have indicated the following conclusions:

1. The difference between the NASA and present approaches comes from prior shape classification and applied shape-dependent formulae.
2. A careful selection of the appropriate formulae can significantly improve the estimate of average cross-sectional area.
3. Plate-shaped formula is quite sensitive to the aspect ratio, and may overestimate the average cross-sectional area of thin plates (MLI fragments).
4. Irregular-shaped formula may provide a better estimate in the calculation of the average cross-sectional area of most of the fragments.

Acknowledgments

We wish to acknowledge Professor Yasuhiro Akahoshi of Kyusyu Institute of Technology and his students for their dedicated assistance in the microsatellite impact experiments. We also wish to acknowledge Mr. Yoshihiro Tsuruda, Mr. Kosuke Sakuraba, Ms. Sachi Morinaga, and Ms. Junko Murakami, graduate students of Kyushu University, for their dedicated assistance in the data analysis.

References

Fucke, W., Sdunnus, H., Klinkrad, H. Population model of small size space debris, Final report. Battelle Institute, ESOC Contract No. 9266/90/D/MD, Frankfurt, Germany, June 1993.

Hanada, T and Liou, J.-C. Comparison of Fragments Created by Low- and Hyper-velocity Impacts. *Adv. Space Res.*, 41(7), 1132-1137, 2008.

Hanada, T., Liou, J.-C., Nakajima, T., et al. Outcome of Recent Satellite Impact Experiments. *Adv. Space Res.*, 44(5), 558-576, 2009a.

Hanada, T., Liou, J.-C., Krisko, P. H., et al. For better calculation of the average cross-sectional area of breakup fragments. Transactions of Japan Society for Aeronautical and Space Sciences, Space Technology Japan 7(ists26), Pr_2_25-Pr_2_30, 2009b.

Johnson, N. L., Krisko, P. H., Liou, J.-C., et al. NASA's new breakup model of EVOLVE 4.0. *Adv. Space Res.* 28(9), 1377-1384, 2001.

Krisko, P. H., Reynolds, R. C., Bade, A., et al. EVOLVE 4.0 User's Guide and Handbook, LMSMSS-33020, Lockheed Martin Space Operations Company, 2000.
Krisko, P. H., Horstman, M., Fudge, M. L. SOCIT4 collisional-breakup test data analysis: With shape and materials characterization. Adv. Space Res. 41(7), 1138-1146, 2008.
Liou, J.-C. An update on recent major breakup fragments. NASA Orbital Debris Quarterly News, Vol. 13, Issue 3, 5-6, 2009.
McKnight, D. S., Johnson, N. L., Fudge, M. L. et al. Satellite orbital debris characterization impact test (SOCIT) series data collection report. Kaman Sciences Corp., Contract NAS 9-19215, Alexandria, VA, April 1995.
McKnight, D. S., Johnson, N. L., Fudge, M. L. et al. Analysis of SOCIT debris data and correlation to NASA's breakup models. Kaman Sciences Corp., Contract NAS 9-19215, Alexandria, VA, July 1995.
Murakami, J., Hanada, T., Liou, J.-C., et al. Micro-satellite impact tests to investigate multi-layer insulation fragments. In: Proceeding of the 5th European Conference on Space Debris, Darmstadt, Germany, March 30 – April 2, 2009 (ESA SP-672, July 2009). ESA Publications Divisions, ESTEC, Noordwijk, The Netherlands, 2009.

Table Captions

Table 1. Summary of microsatellite impact parameters.

Figure Captions

Fig. 1. Applicable regimes to classify fragments into irregular- and plate-shaped when an ellipsoid is assumed as shape.

Fig. 2. Microsatellite impact parameters.

Fig. 3. Target microsatellite selected for experiments 1, 2, and 3.

Fig. 4. Fragment sets from: (left) F, and (right) R.

Fig. 5. Present shape classification of NASA's irregular-shaped fragments from: (left) F, and (right) R.

Fig. 6. Present shape classification of NASA's plate-shaped fragments from: (left) F, and (right) R.

Fig. 7. Difference in the area-to-mass ratio distribution of all fragments from: (left) F, and (right) R.

Fig. 8. Difference in the area-to-mass ratio distribution of NASA's irregular-shaped fragments from: (left) F, and (right) R.

Fig. 9. Difference in the area-to-mass ratio distribution of NASA's plate-shaped fragments from: (left) F, and (right) R.

Fig. 10. An ideal plate and its three orthogonal projection dimensions of x, y, and z.

Fig. 11. Estimate uncertainty in the calculation of the average cross-sectional area of plates using Eq. (2).

Fig. 12. Estimate uncertainty in the calculation of the average cross-sectional area of plates using Eq. (4).

Fig. 13. Estimate uncertainty of the present approach in the calculation of the average cross-sectional area of plates.

Fig. 14. Comparison of measured average cross-sectional area with average cross-sectional area estimated by the two approaches.

Fig. 15. Estimate uncertainty in the calculation of the average cross-sectional area with the two approaches in terms of: (left) the characteristic length (L_C), and (right) thickness (z).

Table 1
Summary of microsatellite impact experiments.

Shot	M_t [g]	M_p [g]	V_{imp} [km/s]	E_{imp}/M_t [J/g]	N_{frag}	Collection Rate [%]
HVI	740	4.03	4.44	53.7	1500	89.9
LVI	740	39.2	1.45	55.7	1500	94.8
1	1300	39.2	1.66	41.5	1300	96.2
2	1283	39.2	1.66	42.0	1000	98.3
3	1285	39.2	1.72	45.1	1500	87.9
F	1515	39.2	1.74	39.2	2400	89.7
R	1525	39.3	1.78	40.8	1250	95.8

M_t = Target mass, M_p = Projectile mass
V_{imp} = Impact velocity, E_{imp} = Impact energy (= $M_p \times V_{imp}^2 /2$)
N_{frag} = Number of fragments collected

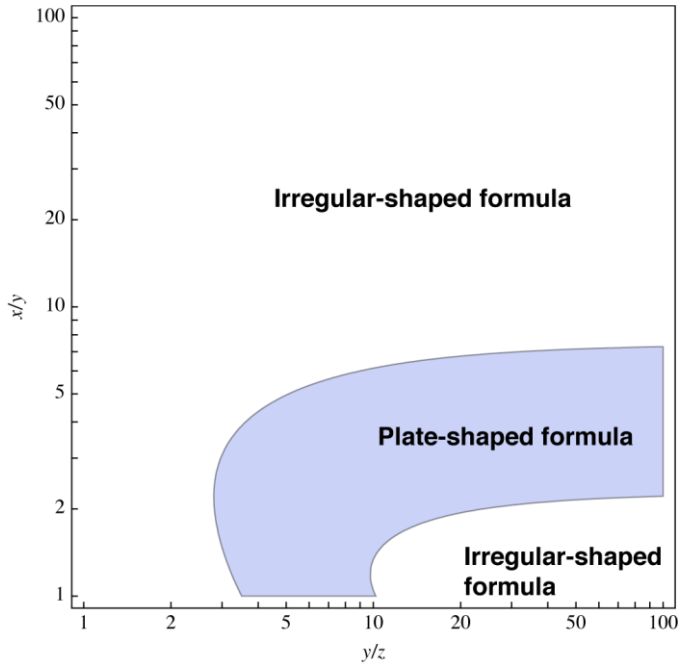
Irregular-shaped formula
Plate-shaped formula
Irregular-shaped formula
x/y
y/z
100
50
20
10
5
2
1
1
2
5
10
20
50
100

Fig. 1

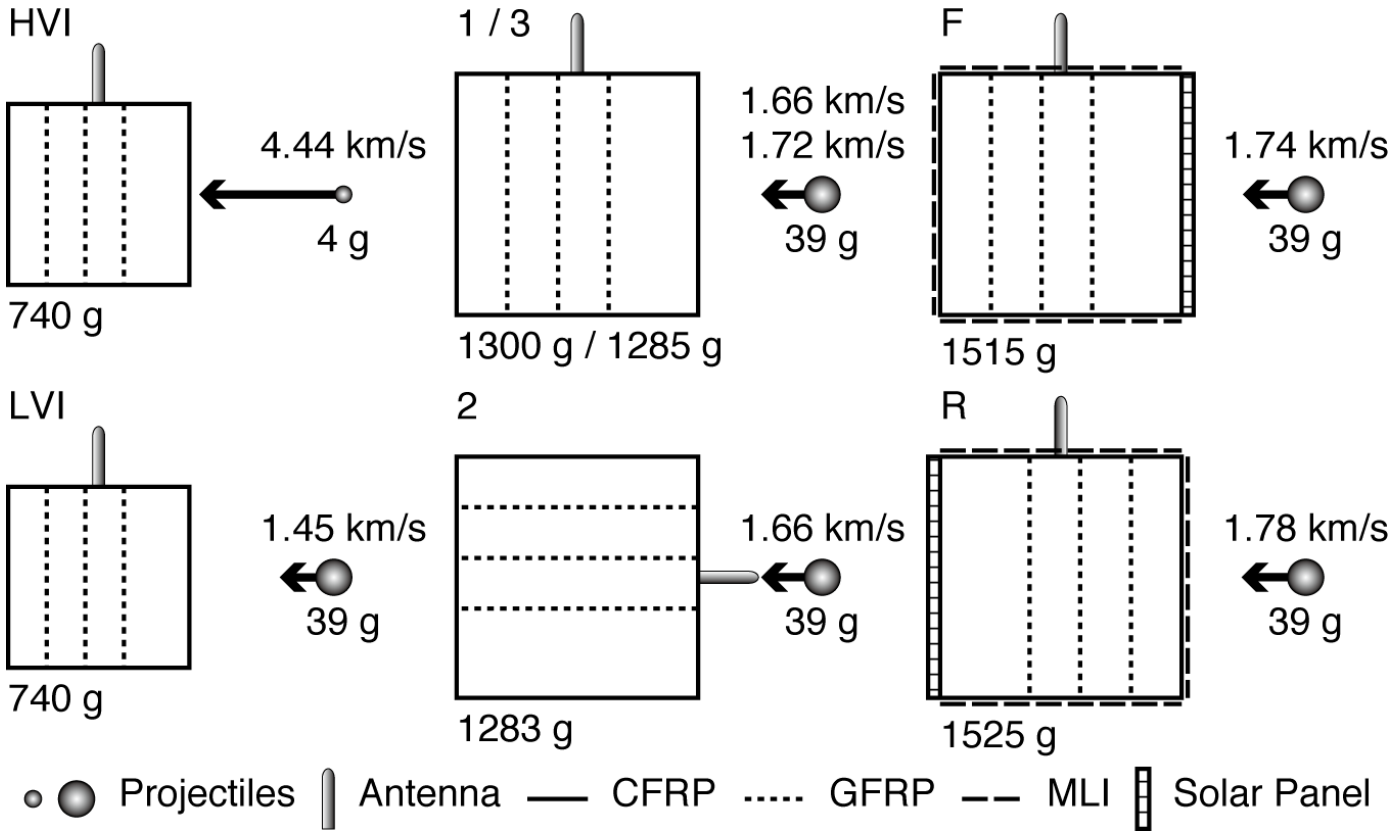
HVI
4.44 km/s
4 g
740 g
1 / 3
1.66 km/s
1.72 km/s
39 g
1300 g / 1285 g
F
1.74 km/s
39 g
1515 g
LVI
1.45 km/s
39 g
740 g
2
1.66 km/s
39 g
1283 g
R
1.78 km/s
39 g
1525 g
Projectiles
Antenna
CFRP
GFRP
MLI
Solar Panel

Fig. 2

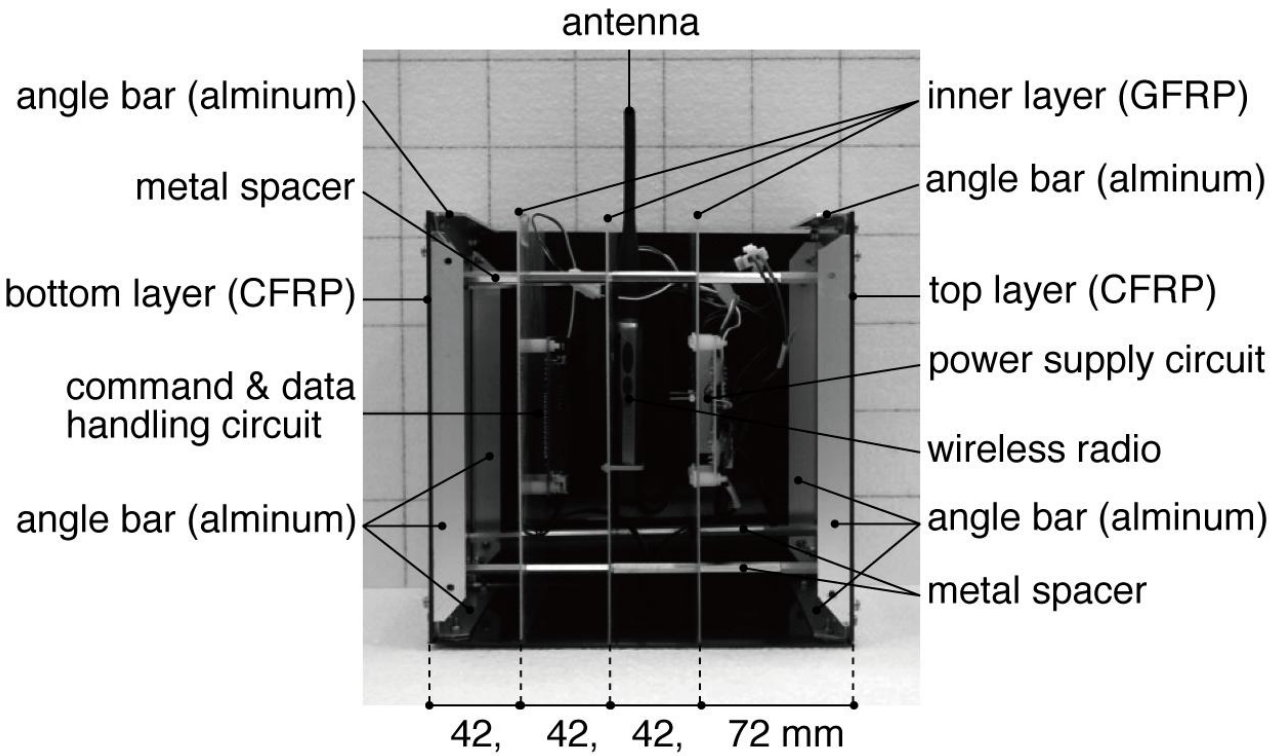
antenna
angle bar (alminum)
metal spacer
bottom layer (CFRP)
command & data handling circuit
angle bar (alminum)
inner layer (GFRP)
angle bar (alminum)
top layer (CFRP)
power supply circuit
wireless radio
angle bar (alminum)
metal spacer
42,
42,
42,
72 mm

Fig. 3

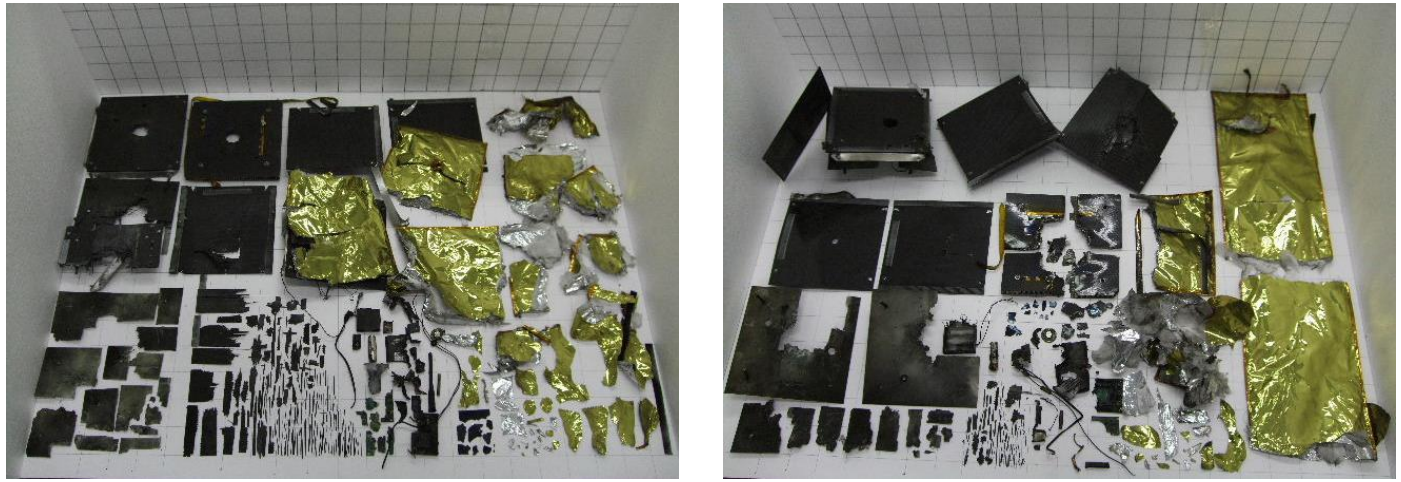

Fig. 4

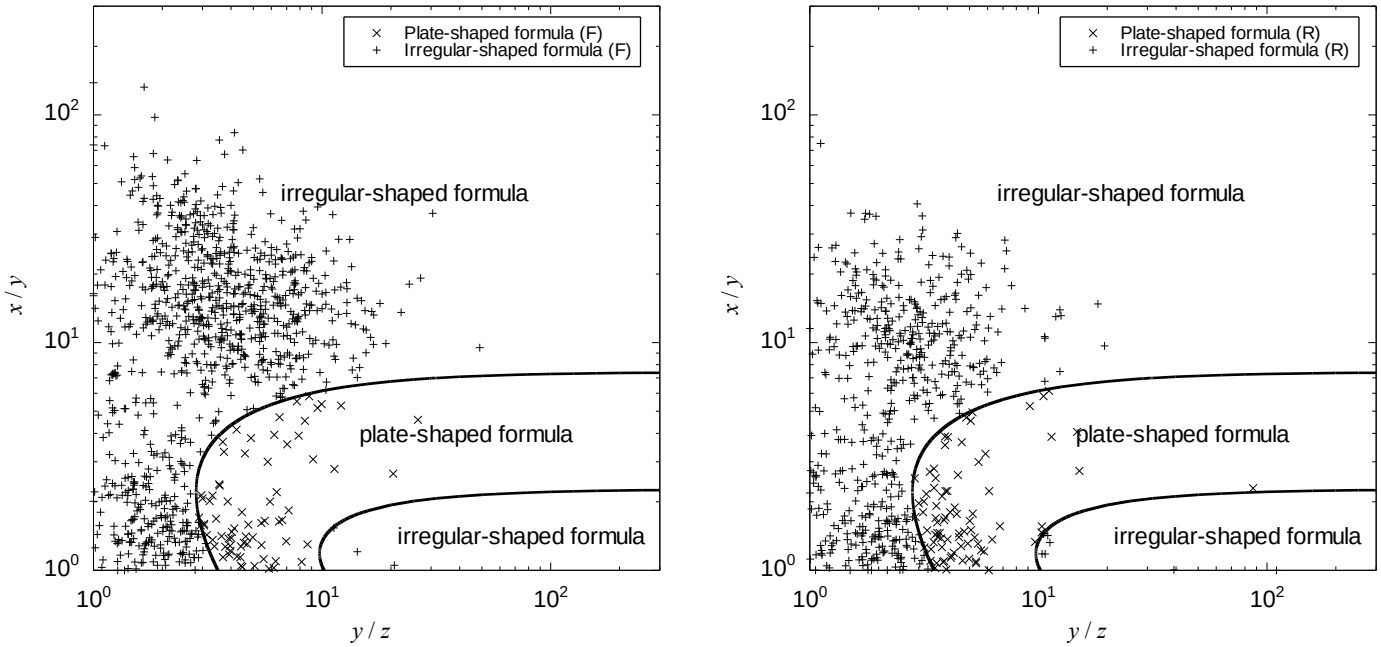
Plate-shaped formula (F)
Irregular-shaped formula (F)
irregular-shaped formula
plate-shaped formula
irregular-shaped formula
x / y
y / z
Plate-shaped formula (R)
Irregular-shaped formula (R)
irregular-shaped formula
plate-shaped formula
irregular-shaped formula
x / y
y / z

Fig. 5

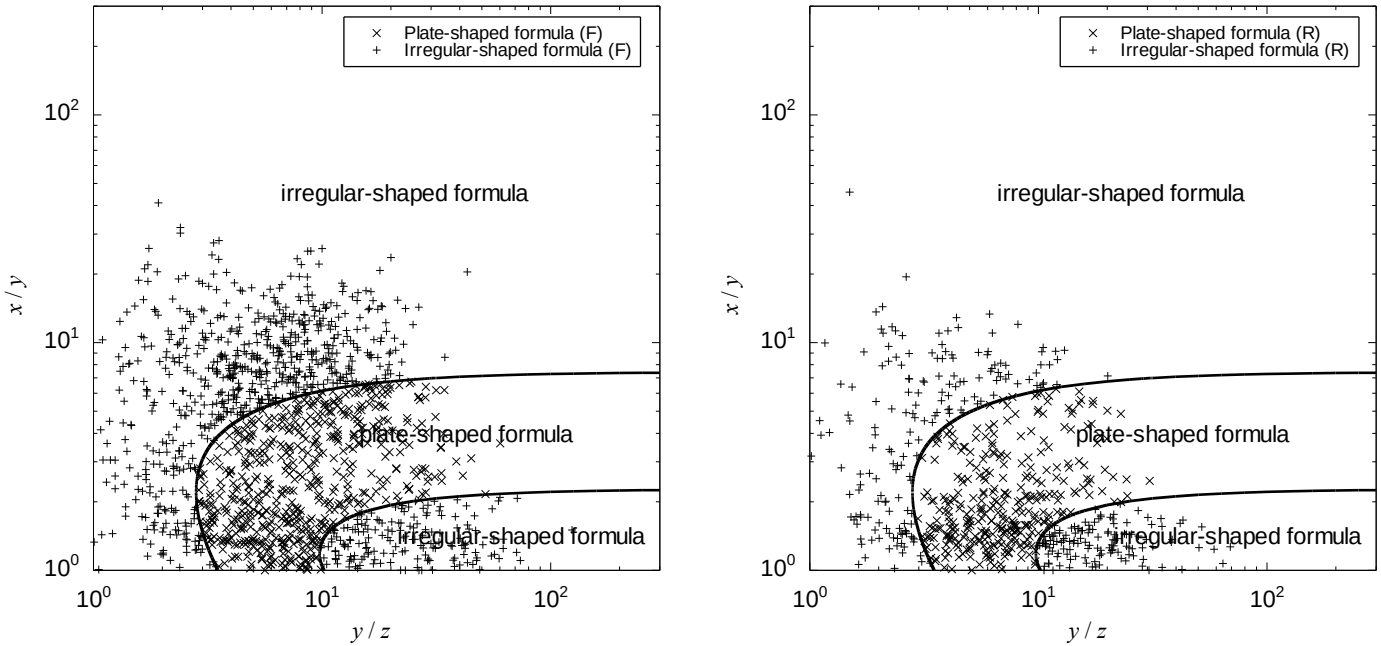
Plate-shaped formula (F)
Irregular-shaped formula (F)
irregular-shaped formula
plate-shaped formula
irregular-shaped formula
x / y
y / z
Plate-shaped formula (R)
Irregular-shaped formula (R)
irregular-shaped formula
plate-shaped formula
irregular-shaped formula
x / y
y / z

Fig. 6

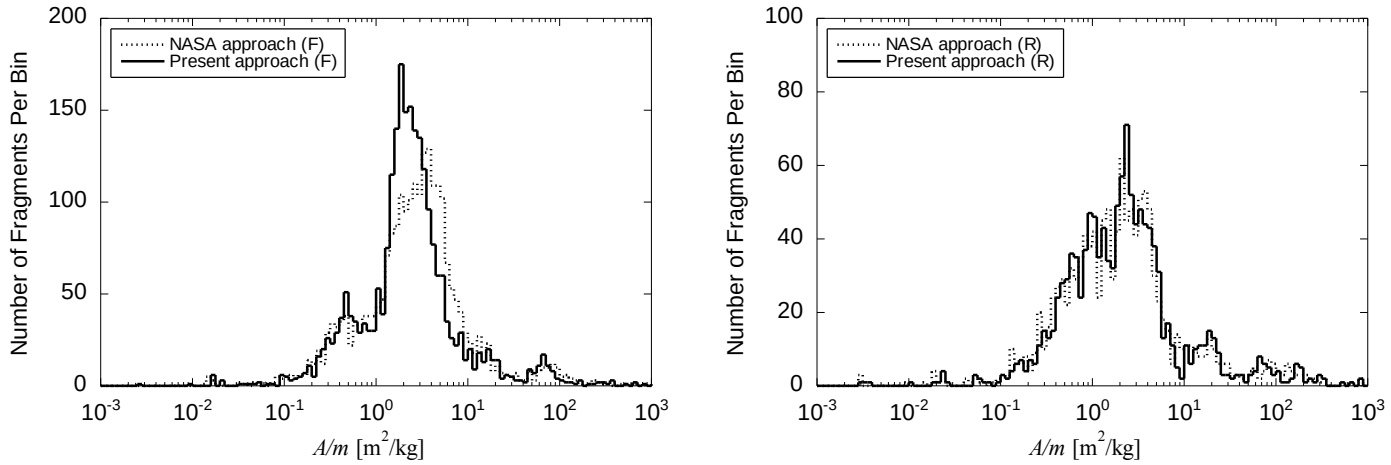
NASA approach (F)
Present approach (F)
Number of Fragments Per Bin
200
150
100
50
0
10^{-3} 10^{-2} 10^{-1} 10^{0} 10^{1} 10^{2} 10^{3}
A/m [m^2/kg]
NASA approach (R)
Present approach (R)
Number of Fragments Per Bin
100
80
60
40
20
0
10^{-3} 10^{-2} 10^{-1} 10^{0} 10^{1} 10^{2} 10^{3}
A/m [m^2/kg]

Fig. 7

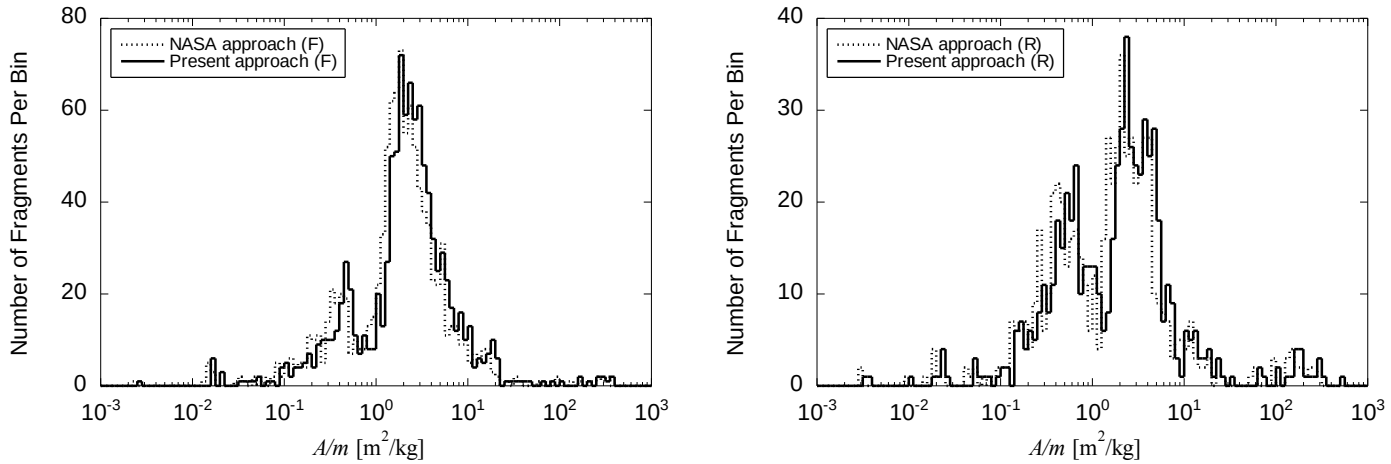
NASA approach (F)
Present approach (F)
Number of Fragments Per Bin
A/m [m2/kg]
NASA approach (R)
Present approach (R)
Number of Fragments Per Bin
A/m [m2/kg]

Fig. 8

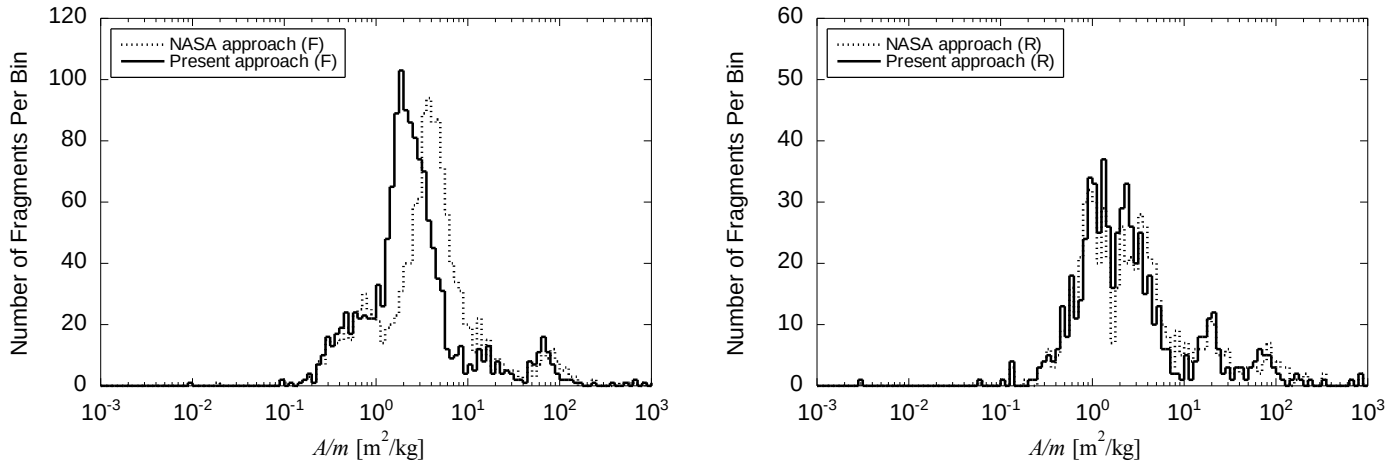
NASA approach (F)
Present approach (F)
Number of Fragments Per Bin
A/m [m²/kg]
NASA approach (R)
Present approach (R)
Number of Fragments Per Bin
A/m [m²/kg]

Fig. 9

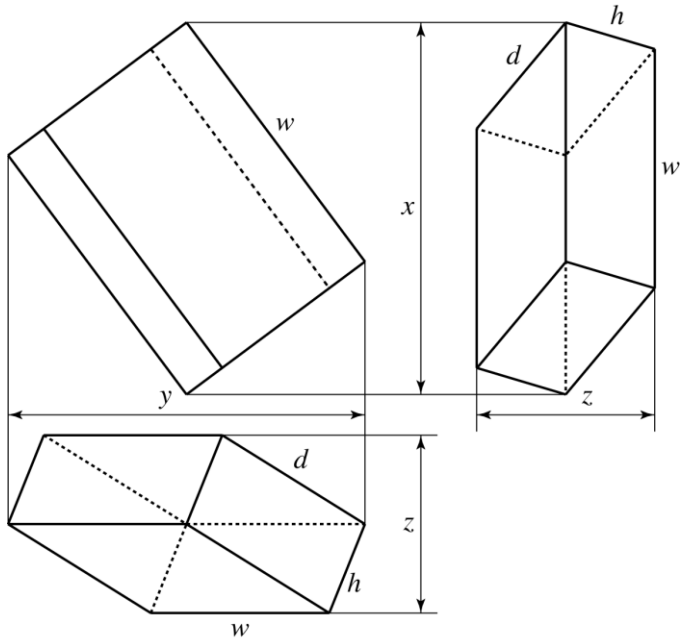

Fig. 10

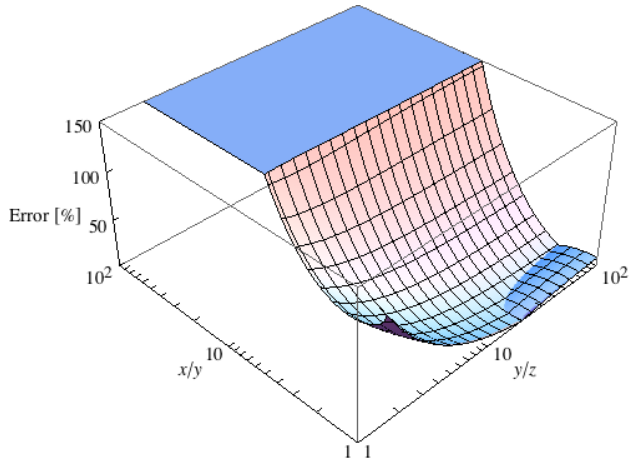

Fig. 11

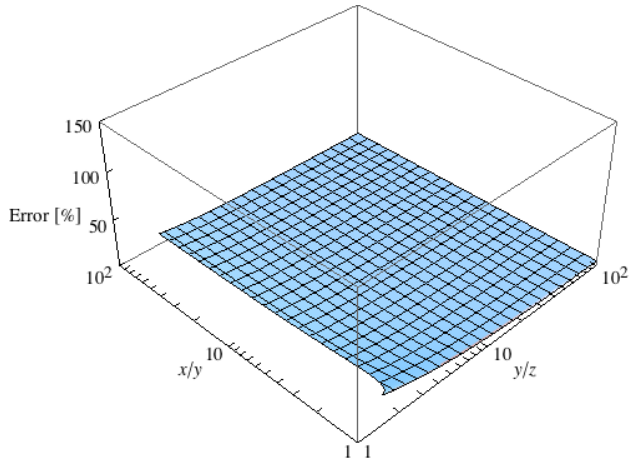

Fig. 12

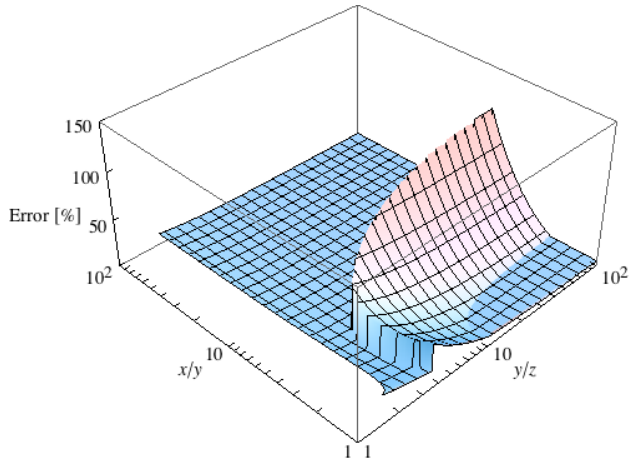

Fig. 13

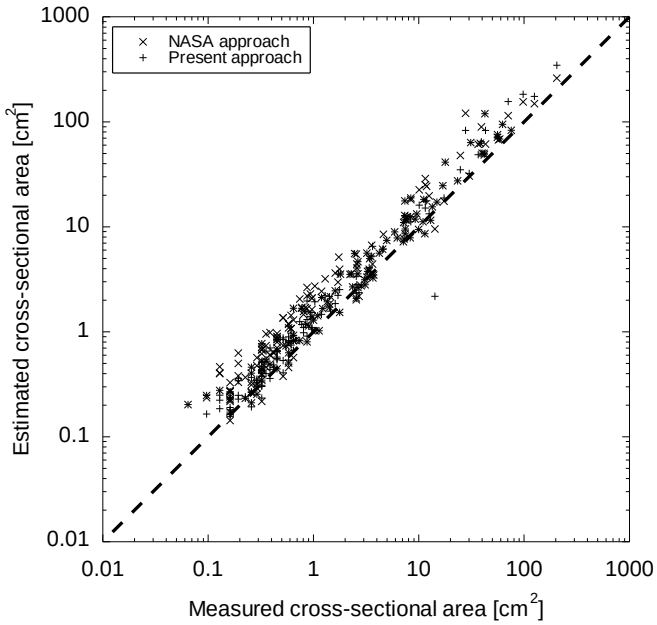
NASA approach
Present approach
Estimated cross-sectional area [cm^2]
Measured cross-sectional area [cm^2]
1000
100
10
1
0.1
0.01
0.01
0.1
1
10
100
1000

Fig. 14

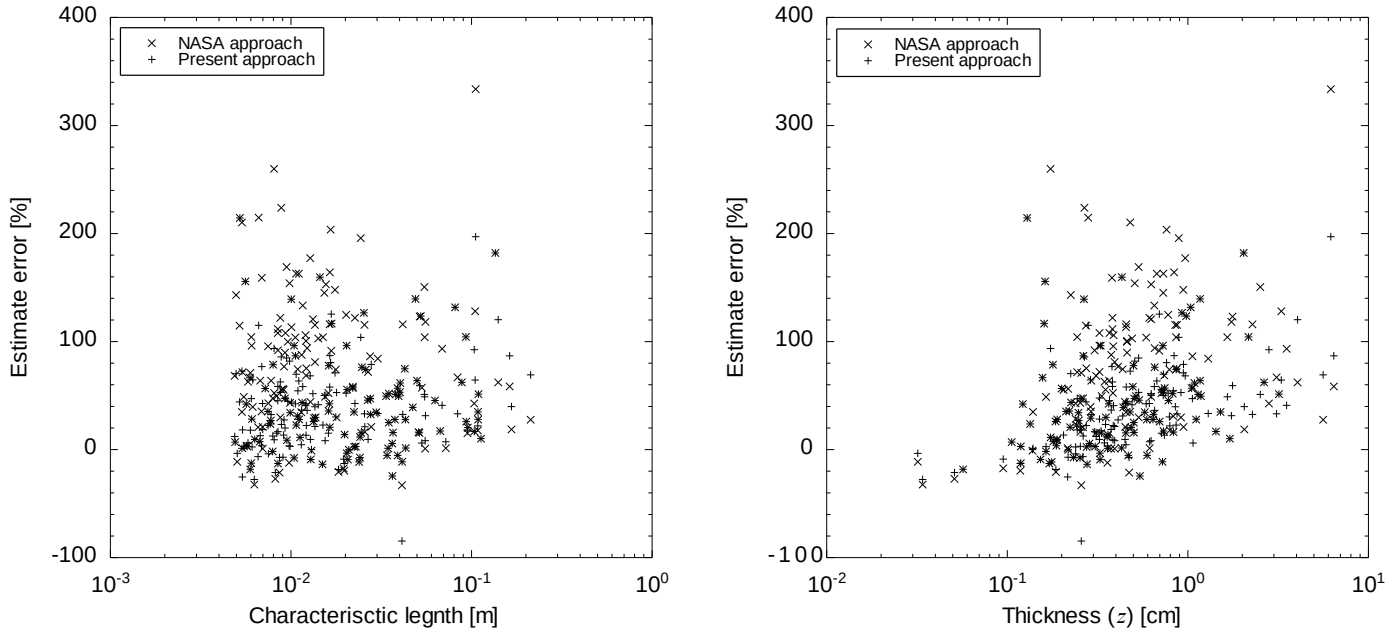
NASA approach
Present approach
Estimate error [%]
Characterisctic legnth [m]
Thickness (z) [cm]

Fig. 15